Modifying the electronic structure of semiconducting single-walled carbon nanotubes by Ar^+ ion irradiation

Antti Tolvanen,[1] Gilles Buchs,[2,3] Pascal Ruffieux,[2] Pierangelo Gröning,[2] Oliver Gröning,[2] and Arkady V. Krasheninnikov[1,4]
[1]*Materials Physics Division, University of Helsinki, P.O. Box 43, FI-00014 Helsinki, Finland*
[2]*EMPA Swiss Federal Laboratories for Materials Testing and Research, Feuerwerkerstrasse 39, CH-3602 Thun, Switzerland*
[3]*Kavli Institute of Nanoscience, Delft University of Technology, P.O. Box 5046, 2600 GA Delft, The Netherlands*
[4]*Laboratory of Physics, Helsinki University of Technology, P.O. Box 1100, FI-02015 Helsinki, Finland*
(Received 11 December 2008; revised manuscript received 20 January 2009; published 25 March 2009)

Local controllable modification of the electronic structure of carbon nanomaterials is important for the development of carbon-based nanoelectronics. By combining density-functional theory simulations with Ar-ion-irradiation experiments and low-temperature scanning tunneling microscopy and spectroscopy (STM/STS) characterization of the irradiated samples, we study the changes in the electronic structure of single-walled carbon nanotubes due to the impacts of energetic ions. As nearly all irradiation-induced defects look as nondistinctive hillocklike features in the STM images, we compare the experimentally measured STS spectra to the computed local density of states of the most typical defects with an aim to identify the type of defects and assess their abundance and effects on the local electronic structure. We show that individual irradiation-induced defects can give rise to single and multiple peaks in the band gap of the semiconducting nanotubes and that a similar effect can be achieved when several defects are close to each other. We further study the stability of defects and their evolution during STM measurements. Our results not only shed light on the abundance of the irradiation-induced defects in carbon nanotubes and their signatures in STS spectra but also suggest a way the STM can be used for engineering the local electronic structure of defected carbon nanotubes.

DOI: 10.1103/PhysRevB.79.125430 PACS number(s): 81.07.De, 61.80.Jh, 07.79.Cz

I. INTRODUCTION

Carbon nanotubes[1,2] possess many fascinating properties,[3] which have motivated extensive research of these systems. Due to their well-defined atomic and unique electronic structures,[4] particular attention has been paid to single-walled carbon nanotubes (SWNTs).[5] Many applications of SWNTs in nanoelectronics are envisaged[6] and SWNT-based electronic devices are even thought to be possible candidates to replace silicon as the basic material in future electronics.[7]

However, as the production of defect-free SWNTs still remains a challenge, possible large-scale implementations of such devices will require a deep understanding of not only perfect SWNTs but also nanotubes with defects. Moreover, defects in SWNTs have been shown to be useful for achieving the desired functionality. In particular, it was demonstrated that intrinsic defects in metallic SWNTs embodied in source-drain-gate devices can provide resonant backscattering characteristics[8,9] leading to low-temperature quantum dot devices, as well as a high gate sensitivity at the defect position.[10] Thus, the knowledge of how and to which extent different types of defects can change the electronic properties of SWNTs is important, as it may open a route toward controllable engineering of the properties of SWNT-based electronic devices or even result in the appearance of a different class of devices with the properties entirely designed by a controlled creation of particular defects.

A widely used method to create defects in carbon nanostructures is the irradiation with energetic particles such as electrons or ions (see Ref. 11 and references therein). Effective changes in the transport properties of nanotubes have been observed after high-dose ion irradiation of nanotubes, showing Coulomb blockade effects.[12–14] More insight into the effect of individual defects on the electronic properties was obtained from low-dose irradiation of SWNTs with 120 eV Ar^+ ions.[15] It was shown that ion-irradiation-induced double vacancies (DVs), in comparison to single vacancies (SVs), strongly reduce the conductivity of metallic tubes. The effects of irradiation in more complicated systems, such as SWNT bundles[16] and films,[17,18] have also been studied and interesting effects such as an increase in the conductance after moderate irradiation dose have been reported.[17]

In the transport experiments discussed above, only indirect information on the type of defects can be deduced. Other experimental techniques which are frequently used to asses the amount of defects in carbon nanomaterials such as Raman spectroscopy,[19–21] x-ray photo electron spectroscopy,[22–24] and electron-spin-resonance method[25,26] provide data which is averaged over many defects. Although transmission electron microscopy[27–30] gives direct information on the atomic structure of defected carbon materials, scanning tunneling microscopy and spectroscopy (STM/STS) is the only experimental technique that allows simultaneous investigations of both the atomic and electronic structures of individual objects down to the subnanometer scale.[31] STM/STS is therefore the ideal tool to study the local modifications of the electronic structure of SWNTs induced by different kinds of defects. This technique has been used to study intrinsic[32,33] and irradiation-induced[34,35] defects in nanotubes and defects at intramolecular junctions.[36,37]

In this work, by combining low-temperature STM/STS experiments with first-principle computer simulations, we study the effects of low-energy Ar-ion-induced defects on the electronic structure of SWNTs. We compare the experimentally measured STS spectra to the computed local density of states (LDOS) of the most typical defects with an aim to

identify the type of experimentally observed defects. We show that the individual irradiation-induced defects can give rise to single and multiple peaks in the gap of the semiconducting nanotubes and that a similar effect can be achieved when several defects are located close to each other.

The paper is organized as follows. A brief description of our experimental techniques is given in Sec. II, while the computational methods used and the simulation setup are described in Sec. III. The experimental and theoretical results as well as their comparison and discussion are presented in Sec. IV. The experimental data on defect stability and interpretations of our observations in terms of defect migration and recombination are presented in Sec. IV H. Finally, we summarize our findings in Sec. V.

II. EXPERIMENTAL TECHNIQUES AND SETUP

A. Low-temperature scanning tunneling microscopy and spectroscopy setup

The experiments have been carried out in a commercial low-temperature STM (Omicron) working in ultrahigh vacuum (UHV) with a base pressure below 10^{-10} mbar and operated at 5 K. The STM topography images have been recorded in the constant current mode. The sample bias was defined as the potential difference of the sample with respect to the tip (sample grounded). We used mechanically cut Pt/Ir tips for the topographic scans and spectroscopy, where the metallic nature of the tips was checked regularly on the conductive substrate. All STM topography images presented in this work have been treated with the WSXM software.[38] The SWNT LDOS can be probed, in the first approximation, by measuring the differential conductance dI/dV at a given position on the tube.[39] Such dI/dV (STS) spectra were measured through the lock-in detection of a low amplitude (5–15 mV) ac tunneling current signal (~600 Hz) added to the dc sample bias under open-loop conditions. The spatial evolution of the defect-induced modifications of the LDOS is studied from the measurement of consecutive and equidistant STS spectra along the tube axis. Typical $dI/dV(x,V)$ data sets, which we call dI/dV scans in the following, consist of 150 dI/dV spectra recorded on topography line scans of 300 points. The spatial extent of a dI/dV scan, which is generally acquired within about 30 min, is always observed to be slightly larger (of the order of 5%) than the spatial extent of the successive (or previous) topography lines acquired within about 0.5 s, due to a dependency of the piezoelectric voltage constant on the scan velocity. In this work, this effect has been systematically corrected by means of a compression of the x scale of the dI/dV scan to allow a consistent comparison between topographic and spatially resolved spectroscopic information on the same nanotube.

Before measuring STS data sets, the metallic nature of the STM tip has been checked on the Au substrate to ensure that the spectroscopy measurements are free from tip artifacts. Furthermore, STS spectra recorded on defect-free portions of the SWNT showed a well-defined electronic gap of the SWNT without any features, indicating that the observed STS features in the SWNT gap are not related to the tip.

B. Sample preparation

Gold-on-glass slides from Arrandee™ (Ref. 40) were used as substrates. In order to obtain Au (111) monatomic terraces, the gold surface was treated by several *in situ* sputtering and annealing cycles, following the same process as described in Ref. 41. The SWNTs grown by the high-pressure CO (HiPco) disproportionation process and then purified[42] were obtained from Rice University. A flake (~50 μg) of HipCo SWNT raw material was sonicated for about 3 h in 1 ml of 1,2-dichloroethane in order to break the van der Waals bundles and obtain a homogeneous colloidal suspension. A droplet of this SWNT suspension was deposited *ex situ* on well-prepared gold substrates with a glass pipette and blown off after about 2 s by a nitrogen gas stream. After introducing the sample in the low-temperature STM system, residues from the solvent of the suspension were removed by annealing the sample to about 390° for a few minutes. STM investigations of the pristine samples revealed individual and bundled-up SWNTs. Typical herringbone structures of the Au(111) surface could still be observed on parts of the sample.

The chiral indexes (n,m) of the investigated SWNTs were determined from the measurements of the chiral angle θ and an estimation of the SWNT band-gap energy from STS spectra[43] compared with the one derived from tight-binding calculations taking into account the curvature effects.[44] For the SWNTs discussed in Secs. IV A and IV H, guesses for the chiral indices are given only if the atomic lattice could be sufficiently well resolved to determine θ.

C. Defect generation

To create defects in nanotube samples, we used a standard Leybold™ ion gun dedicated for UHV sputter cleaning of surfaces, which delivers a rather broad ion beam of about 15 mm in diameter on the sample position. We have investigated the defects created by single-charged Ar^+ ions with kinetic energies of about 200 and 1500 eV. Typical operating parameters of the ion gun are summarized in Table I. These parameters lead to an ion current of 1–2 μA cm^{-2} at the sample position, corresponding to an ion flux of the order of 10^{13} ions cm^{-2} s^{-1}. Based on the desired ion flux on the sample of about 0.1 ion nm^{-2} s^{-1}, an exposure time of the order of 0.1–1 s should be required to achieve a target density of 0.01–0.1 defect sites per nm^2. To achieve such short exposition times, the sample has been moved in and out of the continuous ion beam, making use of the rotational motion of the sample holder.

Similar to the case of proton treatment,[35] the optimal procedure for the irradiation has been calibrated by tests on a highly oriented pyrolytic graphite (HOPG) substrate at room temperature. Optimized parameters for both kinetic energies of the ions used (200 and 1.5 keV) are summarized in Table I. For both cases, the angle between the ion-beam axis and the vector normal to the sample surface have been varied from 0° to about 160° and back to 0° after $T_{exp}=2$ s.

It should be noted here that the ion gun we used does not dispose of an energy filter and the stated ion energies are given by the acceleration voltage with respect to the dc glow

TABLE I. Exposition parameters of the argon-ion gun for standard surface cleaning (row "Standard"), defect generation on SWNTs with kinetic energy 200 eV (row "200 eV") and 1.5 keV (row "1.5 keV"). The following nomenclature is used for the parameters: discharge current (I_d), discharge voltage (V_d), discharge potential (V_p), pressure in the preparation chamber (P_{prep}), and exposition time (T_{exp}). The irradiation has always been performed at room temperature.

	I_d	V_d	V_p	p_{prep}	T_{exp}
Standard	5 mA	600 V	1.5 keV	$\sim 6\times 10^{-6}$ mbar	
200 eV	4 mA	400 V	0 keV	6.1×10^{-5} mbar	≈ 2 s
1.5 keV	1 mA	380 V	1.3 keV	1.1×10^{-5} mbar	≈ 2 s

discharge potential. This means that a considerable energy spreading of about 50–100 eV has to be expected.

III. FIRST-PRINCIPLES ATOMISTIC COMPUTER SIMULATIONS

The atomic and electronic structures of the irradiation-induced defects were studied within the framework of density-functional theory (DFT). We used Vienna *ab initio* simulation package (VASP) (Refs. 45 and 46) plane-wave code, where projector-augmented wave (PAW) (Refs. 47 and 48) potentials were implemented to describe the core electrons and generalized gradient approximation (GGA) by Perdew and Wang[49] for exchange and correlation. As the standard STM cannot detect spin-polarized currents, most of the simulations were nonspin polarized. Several spin-polarized control runs showed that the results do not change qualitatively when spin-polarization effects are taken into account, as demonstrated below.

All structures were relaxed until the forces acting on atoms were less than 0.02 eV Å^{-1}. A kinetic-energy cutoff of 400 eV was found to converge the total energies of our systems within meV. In structural relaxation, a mesh of 9 **k** points was used along the tube axis. After structural relaxation, an electronic relaxation step was performed, converging the electronic structure with more accuracy using 37 **k**-points. The same number of **k** points was used to calculate local density of states and band structures. In DOS calculations, the tetrahedron method with Blöchl corrections[50] was used to integrate over the one-dimensional Brillouin zone.

The simulations were done for the (10,0) nanotube. It was selected as the typical semiconducting nanotube with a diameter close to those observed experimentally. Although most of the experiments were carried out on semiconducting chiral nanotubes, such chiral nanotubes have prohibitively large unit cells which made simulations impossible, while our previous simulations[35] indicated that the effects of defects on the electronic structure are qualitatively the same for both semiconducting chiral and zigzag nanotubes. Nanotubes composed of 2–6 unit cells and having 80–240 atoms were studied.

The use of DFT for calculating defect-induced states in the band gap of various semiconductors has been widely discussed in the literature (see Refs. 51 and 52 for an overview). It is a generally accepted fact that DFT with local-density approximation (LDA) or GGA exchange and correlation functionals frequently underestimates the absolute values of the band gap and may give wrong positions of the defect-induced states in the gap.[52–54] Physically, this is because DFT is inherently a ground-state theory, so that information about excited-state properties (that is the lowest unoccupied state) cannot be rigorously deduced in the absence of any explicit link between ground-state densities and excited-state quantities (the ground-state density uniquely determines the many-body Hamiltonian; that is, information about excited states is, in principle, encoded within the ground-state density). In fact, exchange and correlation effects are not rigorously included in the functionals. There are many theoretical methods[51,52] aimed at improving on the accuracy of the band-gap and defect state calculations, but such simulations are either computationally too expensive (such as GW approximation[55,56] or, to a lesser degree, hybrid functionals[57,58]) or are based on additional approximations, e.g., LDA+U method.[60,59] Although hybrid functional and LDA/GGA+U approaches give for some systems excellent results, the agreement may be fortuitous.[51] However, our situation is somewhat different. Our DFT-GGA calculations give a gap value of 0.74 eV for the (10,0) nanotube, which is quite close to the experimental value of 0.9 eV.[61] Thus one can hope that the positions of the simulated defect-induced states are close to the real ones.

The STS spectra were computed as an average over LDOS corresponding to atoms within a 5 Å distance from the defect center. Physically, such an approach takes into account the tunneling of electrons from/to the STM tip to several atoms closest to the tip.

To ease the comparison to the experimental dI/dV scans, we also computed the LDOS along a line parallel to the tube axis and intersecting a defect in the atomic structure of a SWNT. As the typical sizes of the experimental dI/dV scans were much larger than the simulation cell (about 20 Å long), we augmented the map corresponding to the defected nanotube with 10-nm-long LDOS maps of the pristine system joint at the borders with a Fermi function.

In the LDOS maps, we took into account neither constant current condition of the experimental dI/dV scans, which leads to lateral differences in the intensity of the experimental spectra, nor the voltage-dependent transmission coefficient in STS.[62] However, spectral shapes, width, and energetic position of defect-related states are not significantly affected by this fact, so that a faithful qualitative comparison between simulation and experiment can be made. Although the effects of the constant current condition and the transmis-

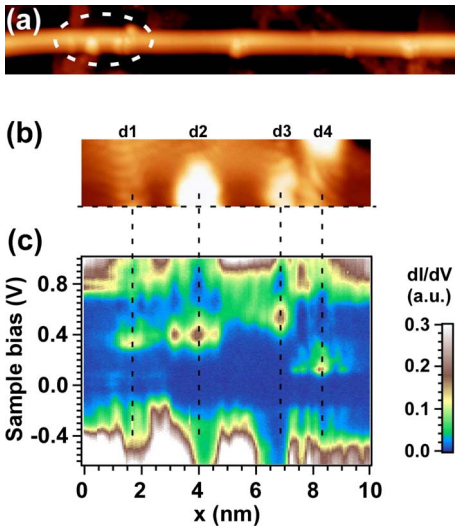

FIG. 1. (Color online) STM/STS images of a 50-nm-long segment of a semiconducting SWNT [(2,9) or (2,10)] exposed to 200 eV Ar ions. (a) STM topography image: U_s=1 V, I_s=0.25 nA, and Δz=1.24 nm. (b) Detailed image of the tube section with defect sites $d1-d4$ inside the dashed ellipse drawn in panel (a). (c) dI/dV scan recorded along the horizontal dashed line. U_s=1 V, I_s =0.25 nA, T=5.3 K, U_{mod}=15 mV, and x_{res}=0.67 nm.

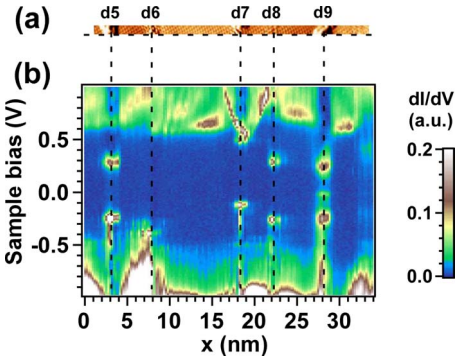

FIG. 2. (Color online) STM/STS images of a segment of a semiconducting SWNT exposed to 200 eV Ar ions. (a) STM topography image with five defect sites $d5-d9$. (b) dI/dV scan recorded along the horizontal dashed line. U_s=1 V, I_s=0.1 nA, T=5.22 K, U_{mod} =15 mV, and x_{res}=0.22 nm.

sion coefficient could be implemented in the simulated maps,[62] we have opted not to do so here and display the plain LDOS because of its fundamental physical nature.

IV. RESULTS AND DISCUSSIONS

A. SWNTs subjected to 200 eV Ar-ion bombardment

Figure 1(a) shows a STM topography image of a 50-nm-long segment of a semiconducting SWNT with chiral indices (2,9) or (2,10) exposed to 200 eV Ar ions. The average defect spacing is about 7 nm and the apparent height of the defect features is ranging from 0.5 to 4 Å, with a lateral extension varying typically between 5 and 30 Å. Figure 1(b) shows a detailed image of the tube section inside the dashed ellipse drawn in Fig. 1(a). A dI/dV scan recorded along the horizontal dashed line is presented in Fig. 1(c). Four defect sites labeled $d1-d4$ are clearly distinguishable and each of them gives rise to spatially localized single peaks in LDOS in the midgap region or in the upper half part of the band gap. Such signatures in the differential conductance are frequently observed in the case of a 200 eV Ar-ion treatment, with full widths at half maximum (FWHMs) ranging from 60 to 200 meV.

A second type of frequently observed features in dI/dV spectra is shown in Fig. 2. The STM topography image of another semiconducting SWNT [either (2,9) or (2,10) SWNT] with five defect sites labeled $d5-d9$ is presented in panel (a). In the lower panel (b), the dI/dV scan recorded along the horizontal dashed line shows double-peak structures for defect sites $d5$, $d8$, and $d9$. The typical characteristic of these double-peak structures is a very symmetric signature regarding intensity and FWHM. The energy splitting between the states is 528, 547, and 485 meV for $d5$, $d8$, and $d9$, respectively. These structures are very similar to the hydrogen dimers-induced symmetric-paired states discussed in Ref. 35. However, an explanation based on a possible hydrogen chemisorption on the SWNT walls during the Ar-ions bombardment can be ruled out, as hydrogen partial pressure was in the 10^{-10} mbar range, measured during the ion bombardment by means of mass spectrometry. The signature of defect $d7$ is a sharp single peak in the gap region, whereas for $d6$ no new state in gap can be observed, but changes in the LDOS in the valence and conduction band. It should be generally marked that one cannot assume that the defect-induced changes in the LDOS are limited to new states in the gap only (although these are very prominent). There are also modifications in the valence-band regions, which however are more extended in energy and difficult to classify.

B. SWNTs subjected to 1.5 keV Ar bombardment

Figure 3 shows the STM topography image and dI/dV scans recorded along two different semiconducting SWNTs irradiated with 1.5 keV Ar ions. Two ($d1-d2$) and four ($d3-d6$) defect sites can be seen in Figs. 3(a) and 3(c), respectively. The defect labeled $d3$ gives rise to a single peak in the midgap region, defect $d6$ to a double-peak structure, while all the other defect sites presented in Fig. 3 show complex multipeak configurations with nonzero intensity almost in the entire gap region. These defects can therefore not be understood as perturbations (e.g., sharp new states) in the LDOS superimposed to a largely unchanged gap structure. Besides, the electronic structure can locally be changed, with a corresponding change in the gap structure (e.g., width). Defects $d4$ and $d5$ in Figs. 3(c) and 3(d) are good illustrations of this situation.

We consider a defect structure as complex if more than two peaks are observed in the corresponding spectra or if the intensity is nonzero in the most part of the gap. Of 34 defect sites investigated for the 200 eV bombardment, we found 8 complex defect structures and of 60 defect sites investigated for 1.5 keV bombardment, we found 27 complex defect structures. We thus observed an increase of about 95% in the complex defect structures (from 23% to 45% of the total

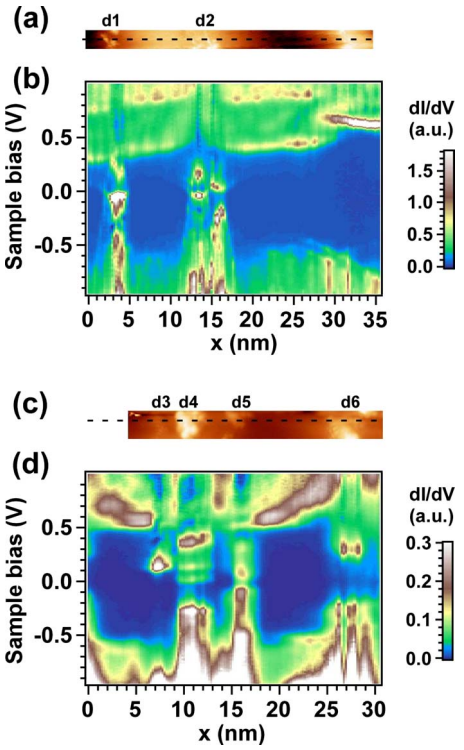

FIG. 3. (Color online) [(a) and (c)] STM topography images of two semiconducting SWNTs irradiated with 1.5 keV Ar ions and [(b) and (d)] the corresponding dI/dV scans recorded along the horizontal black dashed lines. Measurement parameters in (b): U_s =1 V, I_s=0.15 nA, T=5.24 K, U_{mod}=15 mV, and x_{res}=0.24 nm. Measurement parameters in (d): U_s=1 V, I_s=0.1 nA, T=5.2 K, U_{mod}=15 mV, and x_{res}=0.3 nm.

structures) going from the 200 eV to the 1.5 keV treatment. As we discuss below at length, such an increase in the number of complex structures can naturally be understood in terms of a higher number of nearby point defects created by 1.5 keV Ar ions as compared to 200 eV ions.

C. Signatures of irradiation-induced defects in STM images of nanotubes as predicted by first-principles simulations

The analysis of the STM images indicates that the exposure of nanotubes to energetic Ar ions gives rise to the appearance of protrusions in the STM images and that the most commonly observed changes in the electronic structure of SWNTs irradiated with 200 eV ions are single and double-peak structures at various positions in the band gap, while ions with higher energies normally give rise to complex structures. To give an interpretation of these results, it is necessary to discuss first the production of defects in nanotubes under low-energy Ar-ion irradiation.

Our previous molecular-dynamics simulations[63–65] indicate that the most prolific defects which appear in nanotubes under ion irradiation are SVs (Refs. 66 and 67) and DVs,[67,68] respectively, as well as carbon adatoms (CAs) on the nanotube surface.[69] Besides, a number of more complicated defects, such as Stone-Wales (SW) (Ref. 70) and inverse Stone-Wales (ISW) defects (Ref. 71), can appear. The former defects representing two adjacent pentagons and two heptagons can be formed by the incomplete recombination of vacancy-adatom pairs,[72] while the latter appears when two isolated CAs form a dimer on the surface which is then incorporated in the atomic network at the expense of local increase in the diameter and formation of nonhexagonal rings.[71] SW defects are known to be able to appear thermodynamically in mechanically strained nanotubes,[73,74] so that one can expect that the recombination of SV-CA pairs should result in a higher number of SW defects if small mechanical strain is present in the nanotube.

All these defects will appear as protrusions in STM images of defected graphitic structures, as numerous simulations indicate.[75–81] The protrusions can originate from not only the topography of defects (e.g., in case of adatoms) but also defect-induced electronic states with energies close to the Fermi energy.[75–83] The geometry of the protrusions in the *simulated* STM images may vary depending on the atomic structure of the defect[76,79] and make in theory possible to distinguish the defects from each other. However, in the *experimental* STM images the convolution and other effects related to the finite size of the STM tip can smear out the spatial variations, so that the hillocks do not have a well-defined shape,[34] except for very few cases.[84]

Nevertheless, if a defect gives rise to new states in the local density of states of nanotubes or graphene (graphite) then the defect can experimentally be identified by juxtaposing the dI/dV curves measured at the defect and by comparing the curves to the theoretically predicted local density of states.

As nearly all the defects give rise to new states, the defects studied in this work are classified in three classes according to their experimentally detectable features. In the first class are the defects which induce a single peak in the band gap. In the second class, we put the defects which change the width in the band gap due to new states which appear at the band edges but do not induce any isolated states in the band gap. The third class consists of defects which give rise to multiple peaks in the band gap. We also studied the simplest combinations of defects.

D. Single-peak defects

The results for the first class of defects are presented in Fig. 4 which shows LDOS for an SV [Fig. 4(a)], a DV [Fig. 4(b)], and a CA [Fig. 4(c)]. All these defects give rise to a single new peak in the band gap. For the SV and CA defects, the new state has a very small dispersion, with the width of the midgap peak being only 70 meV for SV and 50 meV for CA in the 5 unit-cell system. Even though these defects are almost identical regarding the dispersion and the position of the midgap state, one can see in the simulated dI/dV scans (the rightmost panels in Fig. 4) clear differences in the states below the Fermi level. DVs result in a slightly wider peak in the gap, in agreement with the results of previous DFT simulations.[68] The position of the peak depends also on the orientation of the DV (a DV in zigzag tubes can be oriented perpendicular to the tube axis, when two atoms forming a perpendicular bond are removed, or a tilted bond, forming the "parallel" configuration).

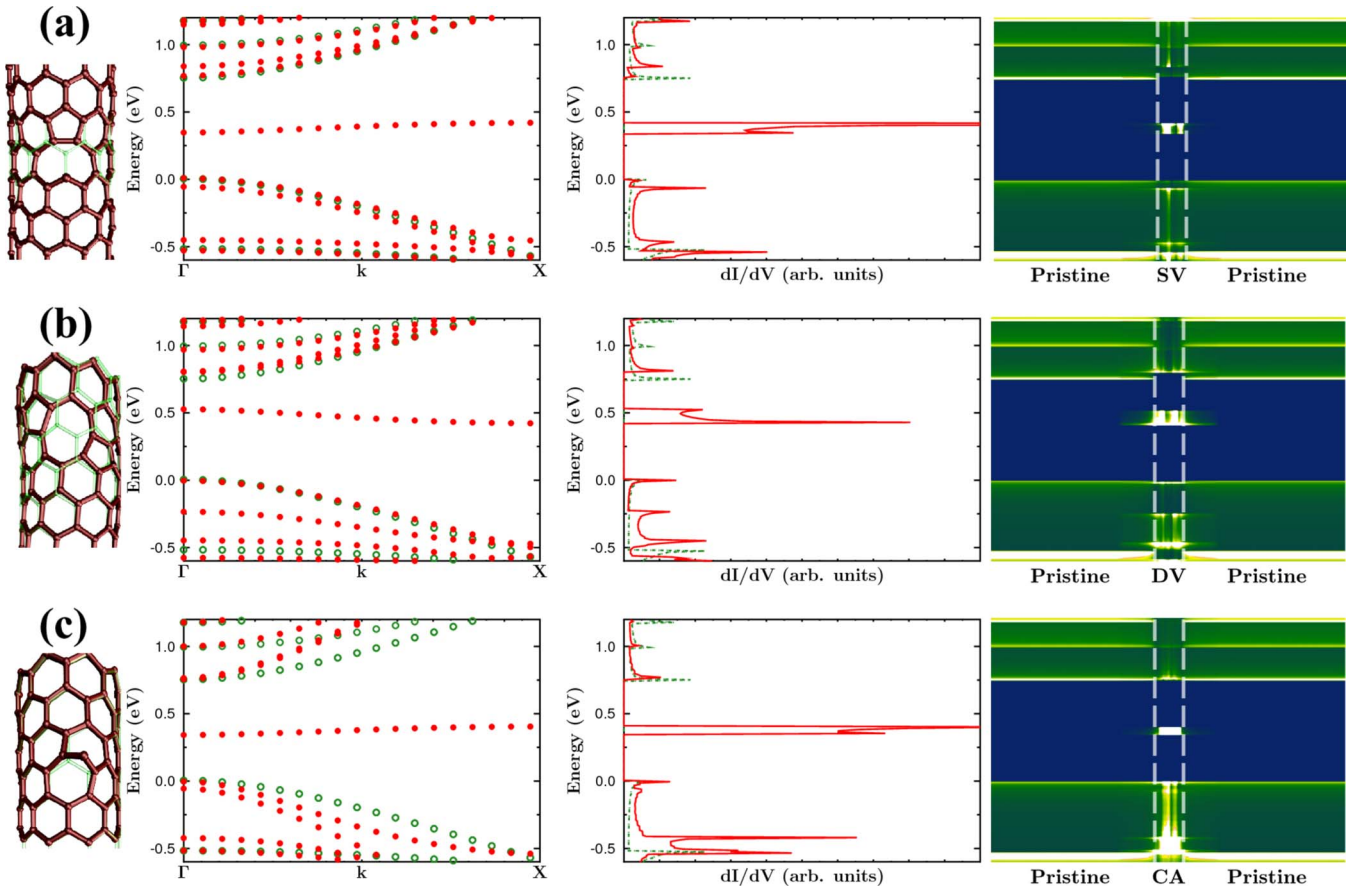

FIG. 4. (Color online) From the left to the right: reconstructed atomic structures of (a) a single vacancy, (b) double vacancy, and (c) a single carbon adatom in the lowest-energy configuration, the corresponding band structures ($\Gamma - X$), local densities of states, and the simulated dI/dV scans. Green bonds and curves correspond to the pristine nanotubes; red to the defected ones. Zero energy corresponds to the valence-band edge of the pristine system.

Carbon adatoms can be in the bridge positions on top of the bond oriented more or less parallel or perpendicular to the tube axis (the actual orientation depends on the chirality of the nanotube, but in armchair and zigzag nanotubes two types of bonds are clearly distinguishable). The parallel position is shown in the inset in Fig. 5. Earlier simulations[69] showed that both configurations are metastable; but when the adatom is on top of the perpendicular bond, such a configuration is lower in energy by 0.4–0.6 eV. Thus one can expect that at low experimental temperatures, CAs should mostly be found in the "perpendicular" configurations. Nevertheless, we calculated the band structure of the other configuration, which is presented in Fig. 5. It is evident that the new defect-induced states which were in the conduction/valence bands for the "perpendicular" configuration are now at the edges of the bands so that the gap width is smaller. The position of the sharp peak is almost the same, but due to the changes in the gap, the peak is now located at the edge of the valence band.

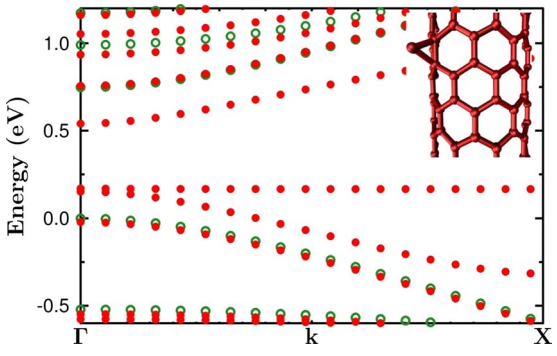

FIG. 5. (Color online) Band structure of a carbon adatom on top of a bond parallel to the tube axis. The inset shows the atomic configuration of this defect. This defect is metastable and higher in energy than that shown in Fig. 4(c).

In a recent study[85] of the transport properties of metallic SWNTs with SVs, it was pointed out that the size of the simulation supercell may affect the position of the midgap peak and thus one has to be careful when stating which changes are due to the defect and which are just simulation artifacts. We did not observe any of these effects caused by the changes in supercell size of the semiconducting systems we studied.

In comparison with the experiment, we can conclude that SV, DV, and CA (in specific orientation) are good candidates to explain the observed single gap peak structures, where modifications in the valence band and conduction band remain relatively small. The origins of these states are single isolated electronic bands with low dispersion in the band gap. In comparison with the experimental results of Figs. 1

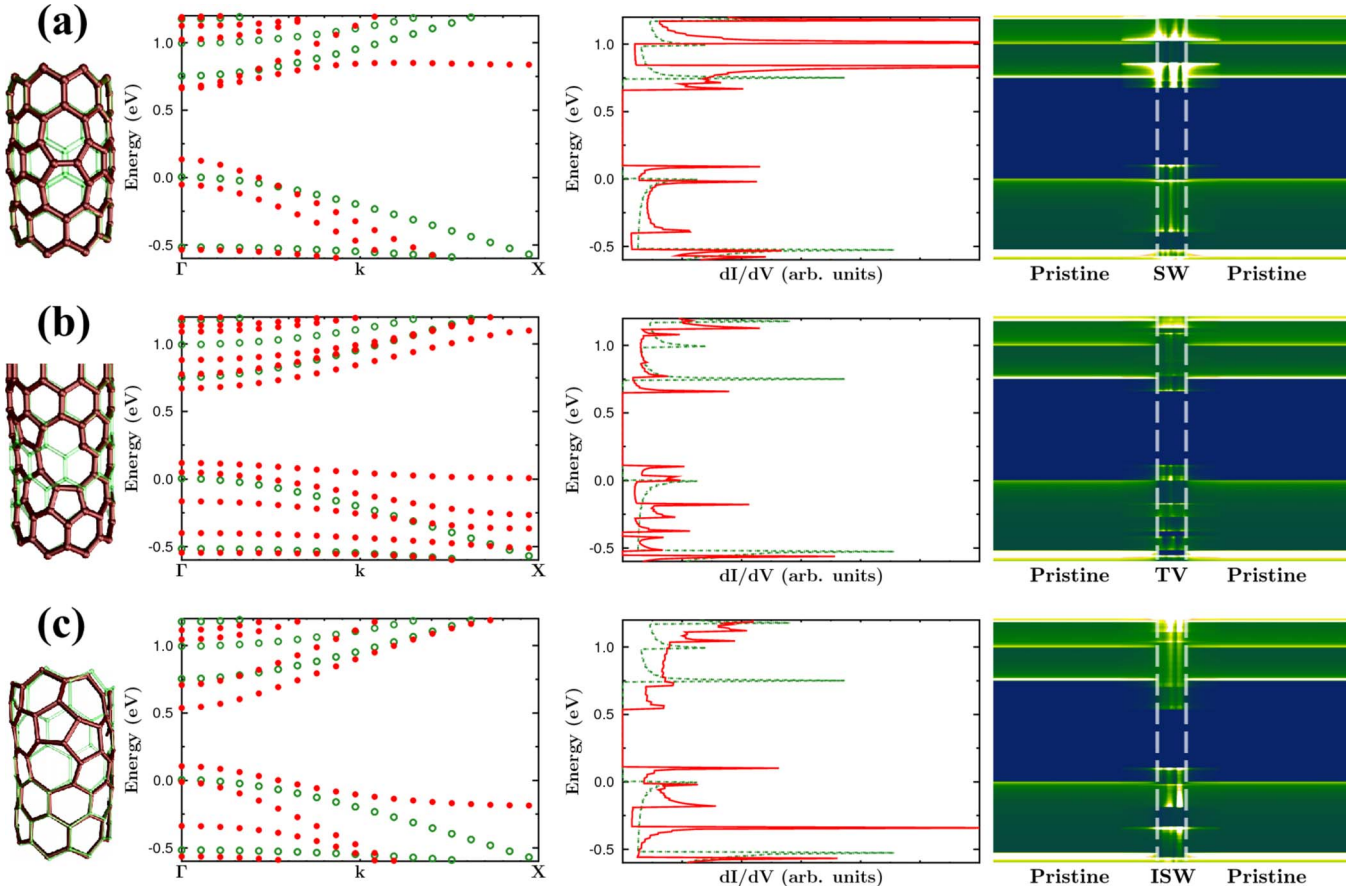

FIG. 6. (Color online) From the left to the right: atomic structures of (a) a Stone-Wales defect, (b) triple vacancy, and adatom dimer (ISW defect) in the lowest-energy configurations, the corresponding band structures ($\Gamma - X$), local densities of states, and the simulated dI/dV scans. Green bonds and curves correspond to the pristine nanotubes; red to the defected ones. Zero energy corresponds to the valence-band edge of the pristine system.

and 2, one needs to take into account that the intensity of the valence band and conduction bands in the STS spectra at the position of the defects is strongly reduced by a measurement artifact. Due to the strong contribution of the defect states to the tunneling current and the fact that the spectra are recorded with constant set point parameter to define the tip-sample distance, the tip on a defect site is retracted by typically 2 Å from the tube,[86] as compared to a pristine portion. This results in a strong reduction in the dI/dV signal from the valence and conduction band and a stronger relative weight of the signal from the defect. Taking this effect into account, we find a good qualitative agreement for the simulated dI/dV scans with the experiment.

E. Band-gap modifying defects

The results for the second class of defects containing triple vacancy (TV), SW, and ISW defect are presented in Fig. 6. These defects modify the width of the band gap due to the appearance of new states at the band edges. As a result, the band gap of the pristine (10,0) SWNT changed from 0.74 to 0.56 eV for the SW and 0.54 for the TV and ISW defects. Similar effects have been reported for semiconducting SWNTs with native SW defects[32] and those created by the tip of an STM.[87] We would also like to note here that SW defects in metallic nanotubes are predicted to give rise to new states in the energy range close to the Fermi level where LDOS is constant.[79,88]

The unambiguous identification of these defects is difficult or impossible (e.g., SW vs ISW) if the distinction is based only on the width of the band gap. At the same time, the additional information which can be retrieved from the spatial variation in the new states in the conduction and valence bands (the rightmost panels in Fig. 6) may be used to identify these defects in the experimental STM images. As evident from the STS maps, the SW defect gives rise to sharp peaks in the conduction band, while the effects of ISW on LDOS are more pronounced in the valence band.

F. Multiple point defects

When the ion energy is close to the optimum value of about 1 keV so that the cross section for defect production is high,[63,65] an ion impact can produce several point defects which are so close to each other that the effects of these defects on the electronic structure of the nanotube cannot be separated. In addition, the adatoms (carbon atoms displaced by the ion and then adsorbed on the tube surface) are mobile at room and lower temperatures[89] and may migrate over the tube surface forming metastable complexes with other

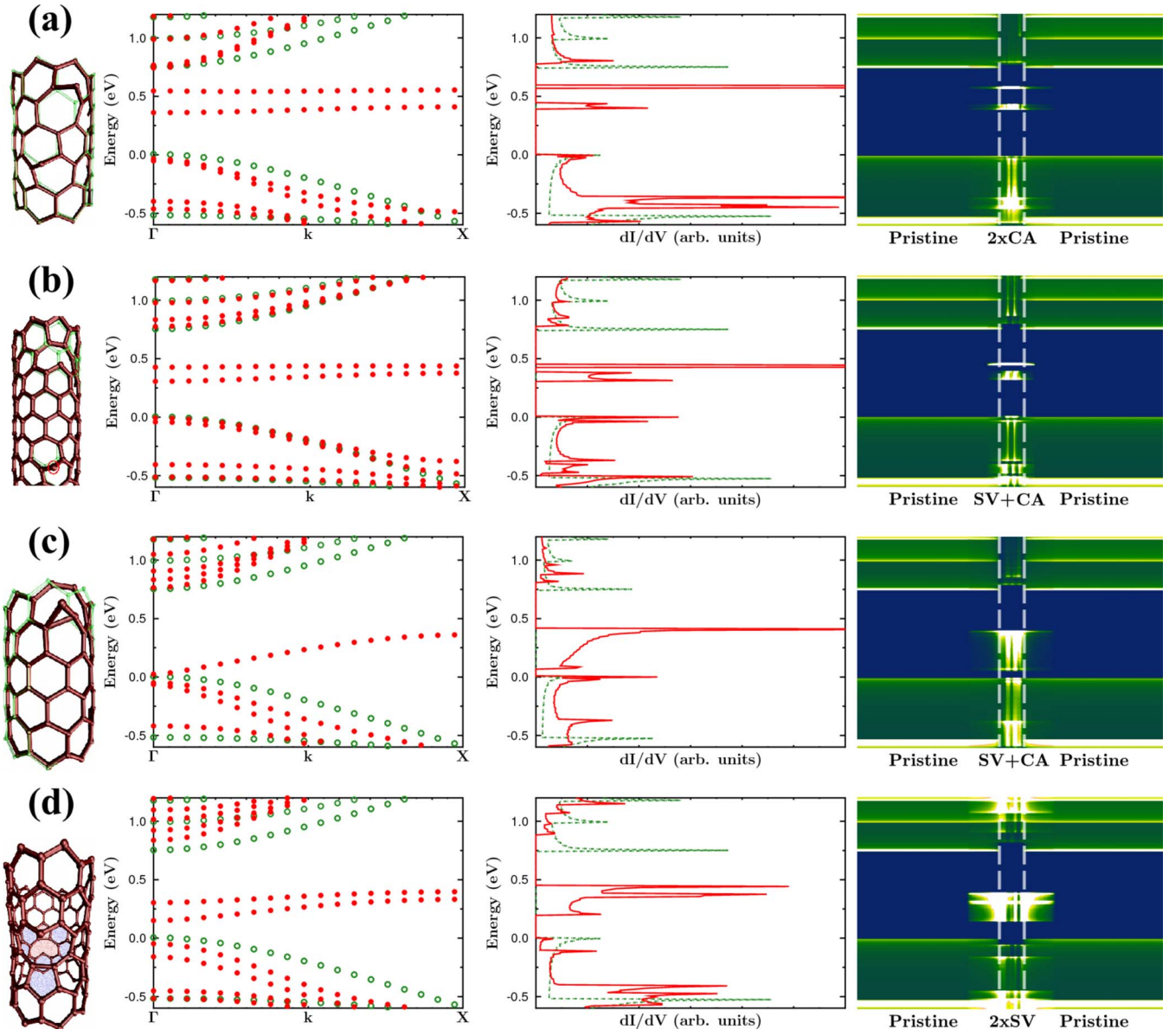

FIG. 7. (Color online) (a) Reconstructed atomic structures of two adatoms, (b) spatially separated and (c) close adatom-single vacancy pair and two single vacancies on the opposite sides of the nanotube (d) in lowest-energy configurations, band structures ($\Gamma - X$), and local densities of states. The Fermi energy of the pristine system is selected as zero in the DOS plot. In (c), the carbon rings forming the defect are colored for clarity.

defects.[90–92] For large multivacancies or even a combination of DVs and SVs, the deformation of the nanotube will be large. The STS signatures associated with several close point defects or multivacancies (see, e.g., defect *d*2 in Fig. 3) produced with 1.5 keV energies may be several nanometers in length. For these reasons, the simulation of these combinations would be computationally very demanding as the simulated system size would have to be at least 10 nm in length leading to ~500 atoms in the simulation cell for the (10,0) SWNT. Due to these restrictions, only combinations of the smallest defects were studied.

The defects which belong to this class are separated CA and CA-SV pairs as well as a system with SVs on the opposite sides of the nanotube. Recently, it was shown that paired electron states can be created in the band gap of semiconducting nanotubes by hydrogen adsorption.[35] The separation of the paired states in the band gap is modulated by the adsorbed hydrogen adatom separation and position in the lattice. For CAs separated by about 5 Å, the effect is similar [see Fig. 7(a)]. Spatially separated CAs induce paired states in the band gap with the separation between the peaks being 0.2 eV. The splitting between the states depends on the separation between CAs and vanishes when CAs are faraway from each other. In case of single vacancies [Fig. 7(d)], the states are not separable due the dispersion of the induced bands within defect separations possible in the 5 unit-cell system we used in our simulation.

Formation of a CA-SV pair is a very likely outcome of the ion impact if the recoil carbon atom receives relatively little kinetic energy from the ion, so that the displaced carbon

atom is not sputtered away, but remains in the system. CA-SV pairs have also been reported to be prolific in graphene under electron irradiation.[27] In Fig. 7(b) we present the atomic and the electronic structures of a SV-CA pair for well-separated (about 10 Å) SV and CA defects. Such SV-CA pair gives rise to two peaks in the LDOS, which can be interpreted as a superposition of the peaks corresponding to isolated SV and CA defects.

The mobility of CAs or SVs may result in a recombination of CA-SV pairs. If there is a finite-energy barrier for the adatom-vacancy annihilation, the recombination may proceed through the formation of a metastable configuration formed by a close CA-SV pair. Such a configuration was recently suggested to explain double-peak structures observed in STS spectra of pristine SWTS.[32] Although an alternative explanation for these features has been put forward,[93] we studied the configuration proposed in Ref. 32 as well. We found that this structure is unstable with respect to forming a configuration with lower symmetry and lower energy. The configuration is shown in Fig. 7(c). It could be interpreted as metastable Frenkel defect, analogously to defects in graphite.[94] The configuration we found does not give rise to double-peak structures in the STS spectra, which confirms that such features cannot be associated with close CA-SV pairs.

If a nanotube is irradiated with Ar ions having energies above ~1.0 keV, the scattering angles of the ions can be very small producing vacancies on the opposite sides of the nanotube as presented in Fig. 7(d) for SVs. Even though the spatial distance of the defects is large (half of the circumference, i.e., 12.3 Å), the new bands formed in the band gap have only a small separation, which leads to a miniband in the middle of the gap.

In our experiments more complex multipeak features have been observed with about 95% higher frequency in 1.5 keV irradiated samples as in 200 eV. Such defect combinations, as seen in Fig. 3, can be qualitatively explained with the simulation results even though the exact structure of these defect combinations is impossible to deduce. Based on the correlation between the experimental results—our previous empirical potential molecular-dynamics simulations on defect production in SWNTs under ion irradiation[63] and DFT simulations of the electronic structure of nanotubes with defects—one can conclude that the multipeak features in the experimental STS spectra should indeed originate mostly from several close point defects.

G. Spin-polarized calculations

Earlier simulations showed that CA and some other defects in nanotubes and other carbon nanomaterials[95,96] can have local magnetic moments. Although the standard STM with the tip made from a nonmagnetic material probes simultaneously the LDOS corresponding to majority and minority spins, an account for magnetism can change the positions of defect-induced peaks.

In order to assess the difference in the electronic structures of defected carbon nanotubes calculated with and without account for spin polarization, we studied in detail two representative cases: single adatom on a (10,0) nanotube [Fig. 4(c)] and two spatially separated adatoms [Fig. 7(a)]. LDOS of nanotubes with the defects calculated with (red curves) and without (green curves) account for spin polarization is presented in Fig. 8. In the spin-polarized calculations, LDOS is a sum of the spin-polarized LDOS for majority and minority spins. It is evident that the account for magnetism gives rise to the splitting of some peaks into two close subpeaks, so that the defect-induced states may look somewhat wider, and it also results in somewhat different intensities of the peaks. However, the picture remains essentially the same. We expect that the same holds for other magnetic defects.

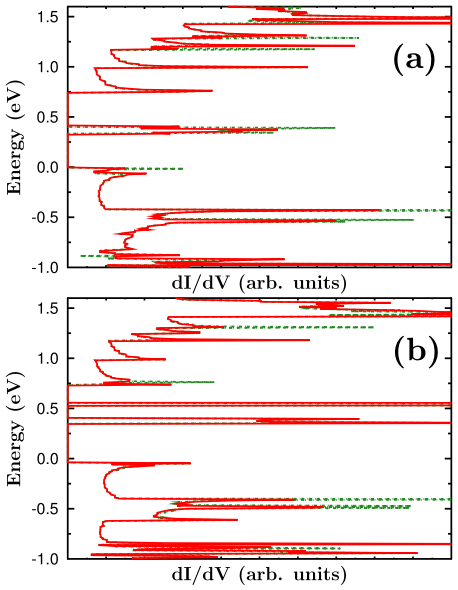

FIG. 8. (Color online) Local densities of states of defected nanotubes calculated with (red curves) and without (green curves) account for spin polarization. In the spin-polarized calculations, LDOS is a sum of the LDOS for majority and minority spins. (a) Single C adatom shown in Fig. 4(c). (b) Two adatoms presented in Fig. 7(a). It is evident that although spin-polarized calculations give rise to a slight broadening of the peaks, the positions and width of the peaks are essentially the same.

H. Defect stability

The reliability of devices based on the local modification of SWNTs by a controlled creation of specific defects should critically depend on the defect stability. In this section, we will describe the changes at the defect sites which we observed under different measurement conditions.

Figure 9 shows three consecutive dI/dV scans recorded on a semiconducting SWNT with three defect sites labeled $d1-d3$ induced by 1.5 keV Ar ions. The dI/dV scans were recorded along the horizontal dashed lines in (a), (c), and (d) at 5.26 K with the following setpoint parameters: $V_s=1$ V, $I_s=0.12$ nA in (b) and $V_s=0.9$ V, and $I_s=0.12$ nA in (d) and (f). The corresponding apparent height profiles recorded along the same lines as for the dI/dV scans are plotted in panels (g)–(i).

In Figs. 9(a) and 9(b), each defect site $d1-d3$ gives rises to different electronic signatures: symmetric paired gap

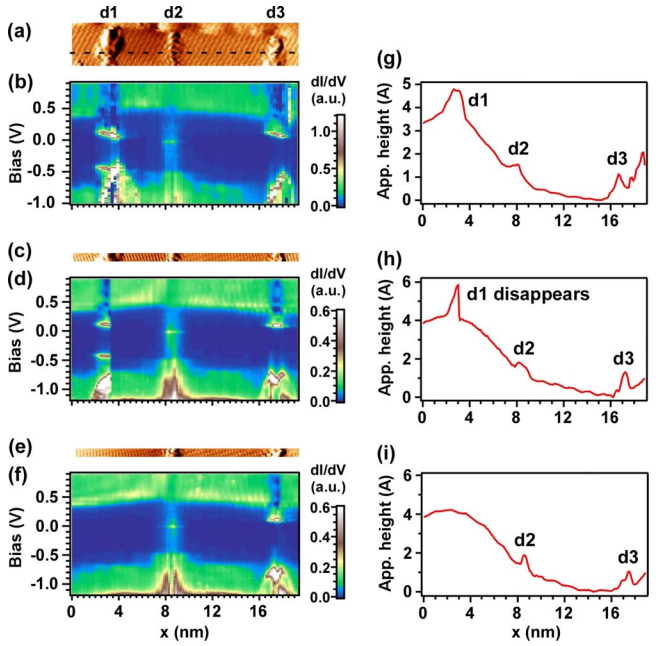

FIG. 9. (Color online) [(a), (c), and (e)] Time sequence of STM images and [(b), (d), and (f)] dI/dV scans recorded along the axis of a semiconducting SWNT (black dashed lines) exposed to 1.5 keV Ar ions. [(g)–(i)] Time sequence of apparent height profiles recorded along the same lines as for the dI/dV scans in (b), (d), and (f). STM parameters for (b): $V_s=1$ V, $I_s=0.12$ nA, $V_{\mathrm{mod}}=16$ mV, $x_{\mathrm{res}}=0.25$ nm, and $T=5.26$ K; for (d) and (f): $V_s=0.9$ V, $I_s=0.12$ nA, $V_{\mathrm{mod}}=16$ mV, $x_{\mathrm{res}}=0.15$ nm, and $T=5.26$ K.

states for $d1$, nonzero intensity across the entire gap with a single peak at the midgap level for $d2$, and a structure with nonsymmetric paired peaks for $d3$. In Fig. 9(d), one can observe that the defect structure $d1$ has disappeared during the recording of the dI/dV scan, where about only a half of the spatial extent of the paired gap states is visible, followed by a sharp transition to the unperturbed electronic structure. This sharp transition is also clearly visible in the corresponding apparent height profile in Fig. 9(h). The third dI/dV scan in Fig. 9(f) and the corresponding apparent height profile in Fig. 9(i)—both recorded immediately after the second dI/dV scan in Fig. 9(d)—confirm the complete disappearance of the defect structure, leaving the underlying lattice unperturbed.

It is important to notice that both peaks in the STS of defect structure $d1$ vanish simultaneously and completely, leaving the intact structure, as can be inferred from the STM topography and STS spectroscopy. The concerted disappearance indicates that the two peaks should not be considered as the coincidental superposition of two single-peak structures but that they belong to a unity. The fact that this defect can be made to disappear completely indicates that it is only weakly coupled to the nearly pristine tube. This description fits very well with the proposed origin of a pair of interacting carbon adatoms or a carbon adatom and a nearby vacancy, which can completely recombine.

Figure 10 gives an illustration for the case where defect sites experience a modification in their structure. Here, three consecutive STM images (from top to bottom) of a semiconducting (7,5) SWNT exposed to 200 eV Ar ions are displayed. These images have been recorded at $T=5.35$ K with setpoint parameters $V_s=1$ V and $I_s=0.3$ nA. In the top image of panel (a), four defect sites labeled $d1$–$d4$ are visible and single point spectra have been recorded on each of them at positions 1–4. The corresponding spectra are displayed in panels (d)–(g), showing paired gap states for positions 1 and 2 and single gap states for 3 and 4. As discussed above, the double-peak structures can be attributed to two (or more) close but separated CAs or CAs and SVs, and single peaks can be due to single C adatoms, SVs, or DVs. A comparison between the top and middle STM images in panels (a)–(c) clearly shows a modification in the structure of defect $d1$ which splits into two defect sites indicated by positions 1a′ and 1b′. Spectroscopic signatures in panel (d) show a single intense peak at the conduction-band edge for 1a′ and also a single peak at the same energy position but less intense for 1b′. This modification in the structure of $d1$ occurred between the recording of the top and middle images. All other defect structures remain unchanged.

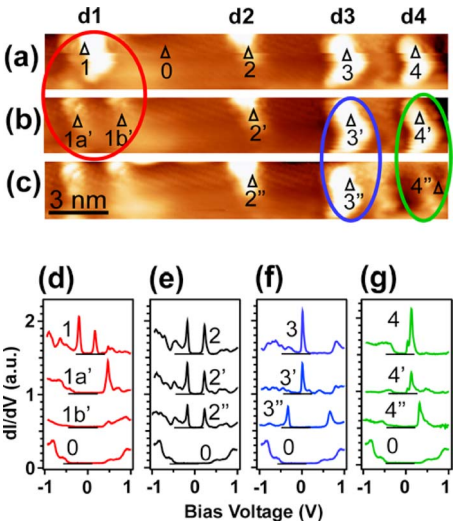

FIG. 10. (Color online) Consecutive topography STM images (line by line flattened) of a semiconducting (7,5) SWNT exposed to 200 eV Ar ions with changes in the defect structure after scanning at higher setpoint current (defects labeled $d1$ and $d3$) or spectroscopy with increasing setpoint currents on individual defect sites ($d4$ and $d5$). Point $d2$ corresponds to the pristine nanotube. [(d)–(g)] Individual spectra recorded on the SWNT at locations indicated by black triangles. $V_s=1$ V, $I_s=0.3$ nA, and $T=5.35$ K.

On defect $d3$, a series of spectra has been recorded at different setpoint currents [in topography image (b)] for the same bias voltage of 1 V. We could observe that this defect structure remained stable up to a current of about 300 nA and changed its structure only at the maximal available current of about 330 nA, with a transition in the electronic structure from a single midgap peak to paired peaks (one in the conduction band and the second in the valence band) as shown in spectra 3′ and 3″ in panel (f). Besides this change, it can be observed that the structure of the nearby defect site $d4$ has also undergone a modification during the same measurement at 330 nA, with a shift of the initial midgap peak toward the conduction-band edge as shown in spectra 4′ and 4″ in panel (g).

Based on our observations, we can classify the typical defect evolution into three categories.

(i) Defect structures with double peaks can disappear from the tube surface after a certain time (few seconds up to tens of minutes) under scanning with standard setpoint parameters of $V_s=1$ V and $I_s=0.1-1$ nA, which correspond to a dissipated power of 0.1–1 nW.

(ii) Defect sites can also change their configuration under scanning with standard setpoint parameters, e.g., in the transition from a double-peak structure on a single defect site to two defect sites each showing a single peak at the conduction band as in Fig. 10(d).

(iii) A defect site showing a single gap state close to the midgap level remained stable with setpoint parameters $V_s=1$ V and $I_s \simeq 300$ nA and changed its structure with a setpoint current of 330 nA. This event has been accompanied by a change in the structure of a close defect site (about 3 nm) showing a shift of midgap peak toward the conduction band.

The order reflects a hierarchy in the stability of the observed defect structures. (i) and (ii) refer to the less stable configurations. The disappearance of defect sites characterized by a double-peak structure in the LDOS during the scan with standard conditions (i) can be explained on the basis of our simulation by the recombination of a CA-SV pair. Another probable scenario is the disappearance of CA-CA structures due to tip-adatom interactions whose nature is similar as in the case of controlled manipulation of weakly adsorbed molecules on metallic surfaces.[97] Note however that in our case the topography signal never showed any typical signature for an adsorption of the adatoms on the tip, indicating a possible desorption of the adatoms or a tip-induced diffusion out of the scanning range.[98]

Generally, the change in configuration referred in (ii) can also be understood from the arguments in (i). Change in the separation between two CAs or migration of two nonadjacent SV-type defects cannot be ruled out since CAs on the outer surface of small-diameter SWNTs and SVs have roughly the same mobility.[67]

The defect site showing a high stability described in (iii) is thought to be a double vacancy. This assumption is based on the measured electronic structure showing an intense and narrow midgap state, which is in good agreement with our calculations for a double vacancy in a (10,0) SWNT. Furthermore, a value for the migration barrier of a double vacancy of more than 5 eV has been recently reported. For comparison, the migration barrier of a SV has been calculated to be about 1 eV (Ref. 67) and 0.5–0.7 eV for a C adatom on the outer shell of a SWNT.[69] Thus, stable double vacancies can be obtained from the coalescence of single vacancies through heating.

V. SUMMARY AND CONCLUSION

In this work we combined first-principles simulations with STM investigation of SWNTs subjected to Ar-ion irradiation to study the changes in the electronic structure of SWNTs due to defects produced by the energetic ions. We showed that individual irradiation-induced defects can give rise to single and multiple peaks in the gap of the semiconducting nanotubes and that a similar effect can be achieved when several defects are close to each other. Our theoretical results make it possible to identify the most typical defects in semiconducting nanotubes by comparing their signatures in the measured STS spectra to the computed density of states. Based on the results of our first-principle simulations of the local electronic structure of semiconducting nanotubes with defects, our experimental data on the abundance of single- and multiple-peak defects confirm a higher production of several close point defects at ion energies of about 1 keV as compared to that at 200 eV, in line with the results of previous empirical potential calculations. We further studied the stability of defects and their evolution during STM measurements. We showed that by manipulating the imaging conditions, one can locally cause recombination or transformations of defects. Our results not only shed light on the abundance of the irradiation-induced defects in carbon nanotubes and their signatures in the STS spectra but also suggest a way on how STM can be used for engineering the local electronic structure of defected carbon nanotubes. Our results can have important implications in SWNT-based photonics and quantum optics in the light of recent observations of exciton localization in SWNTs due to the presence of disorder.[99]

ACKNOWLEDGMENTS

The authors would like to thank R. M. Nieminen and K. Nordlund for useful discussions. This work was supported by the Academy of Finland under CONADEP, OPNA projects, and the Centre of Excellence program and the Swiss National Center of Competence in Research MANEP. We are also indebted to the Finnish IT Center for Science for generous grants of computer time.

[1] S. Iijima, Nature (London) **354**, 56 (1991).
[2] A. Oberlin, M. Endo, and T. Koyama, J. Cryst. Growth **32**, 335 (1976).
[3] R. H. Baughman, A. A. Zakhidov, and W. A. de Heer, Science **297**, 787 (2002).
[4] J. Charlier, X. Blase, and S. Roche, Rev. Mod. Phys. **79**, 677 (2007).
[5] S. Iijima and T. Ichihashi, Nature (London) **363**, 603 (1993).
[6] P. Avouris, Z. Chen, and V. Perebeinos, Nat. Nanotechnol. **2**, 605 (2007).
[7] P. L. McEuen, Nature (London) **393**, 15 (1998).
[8] M. Bockrath, W. Liang, D. Bozovic, J. H. Hafner, C. M. Lieber, M. Tinkham, and H. Park, Science **291**, 283 (2001).
[9] T. Maltezopoulos, A. Kubetzka, M. Morgenstern, R. Wiesendan-

ger, S. G. Lemay, and C. Dekker, Appl. Phys. Lett. **83**, 1011 (2003).
[10] Y. Fan, B. R. Goldsmith, and P. G. Collins, Nature Mater. **4**, 906 (2005).
[11] A. V. Krasheninnikov and F. Banhart, Nature Mater. **6**, 723 (2007).
[12] M. Suzuki, K. Ishibashi, K. Toratani, D. Tsuya, and Y. Aoyagi, Appl. Phys. Lett. **81**, 2273 (2002).
[13] K. Maehashi, H. Ozaki, Y. Ohno, K. Inoue, K. Matsumoto, S. Seki, and S. Tagawa, Appl. Phys. Lett. **90**, 023103 (2007).
[14] K. Ishibashi, D. Tsuya, M. Suzuki, and Y. Aoyagi, Appl. Phys. Lett. **82**, 3307 (2003).
[15] G. Gómez-Navarro, P. J. De Pablo, J. Gómez-Herrero, B. Biel, F. J. Garcia-Vidal, A. Rubio, and F. Flores, Nat. Mater. **4**, 534 (2005).
[16] H. Stahl, J. Appenzeller, R. Martel, P. Avouris, and B. Lengeler, Phys. Rev. Lett. **85**, 5186 (2000).
[17] V. Skákalová, A. B. Kaiser, Z. Osváth, G. Vértesy, L. P. Biró, and S. Roth, Appl. Phys. A: Mater. Sci. Process. **90**, 597 (2008).
[18] V. Skákalová, A. B. Kaiser, U. Dettlaff, K. Arstila, A. V. Krasheninnikov, J. Keinonen, and S. Roth, Phys. Status Solidi B **245**, 2280 (2008).
[19] A. Jorio, M. A. Pimenta, A. G. Souza Filho, R. Saito, G. Dresselhaus, and M. S. Dresselhaus, New J. Phys. **5**, 139 (2003).
[20] M. S. Dresselhaus, G. Dresselhaus, R. Saito, and A. Jorio, Phys. Rep. **409**, 47 (2005).
[21] S. Malola, H. Häkkinen, and P. Koskinen, Phys. Rev. B **77**, 155412 (2008).
[22] B. Ni, R. Andrews, D. Jacques, D. Qian, M. B. J. Wijesundara, Y. Choi, L. Hanley, and S. B. Sinnott, J. Phys. Chem. B **105**, 12719 (2001).
[23] D. Q. Yang, J. Rochette, and E. Sacher, Langmuir **21**, 8539 (2005).
[24] C. Morant, J. Andrey, P. Prieto, D. Mendiola, J. M. Sanz, and E. Elizalde, Phys. Status Solidi A **203**, 1069 (2006).
[25] F. Beuneu, C. l'Huillier, J.-P. Salvetat, J.-M. Bonard, and L. Forró, Phys. Rev. B **59**, 5945 (1999).
[26] A. R. Adhikari, M. B. Huang, H. Bakhru, S. Talapatra, P. M. Ajayan, and C. Y. Ryu, Nucl. Instrum. Methods Phys. Res. B **245**, 431 (2006).
[27] A. Hashimoto, K. Suenaga, A. Gloter, K. Urita, and S. Iijima, Nature (London) **430**, 870 (2004).
[28] K. Suenaga, H. Wakabayashi, M. Koshino, Y. Sato, K. Urita, and S. Iijima, Nat. Nanotechnol. **2**, 358 (2007).
[29] J. C. Meyer, C. Kisielowski, R. Erni, M. D. Rossell, M. F. Crommie, and A. Zettl, Nano Lett. **8**, 3582 (2008).
[30] M. H. Gass, U. Bangert, A. L. Bleloch, P. Wang, R. R. Nair, and A. K. Geim, Nat. Nanotechnol. **3**, 676 (2008).
[31] R. Wiesendanger, *Scanning Probe Microscopy and Spectroscopy. Methods and Applications* (Cambridge University Press, Cambridge, Great Britain, 1994).
[32] S. Lee, G. Kim, H. Kim, B.-Y. Choi, J. Lee, B. W. Jeong, J. Ihm, Y. Kuk, and S.-J. Kahng, Phys. Rev. Lett. **95**, 166402 (2005).
[33] W. Clauss, D. J. Bergeron, M. Freitag, C. L. Kane, E. J. Mele, and A. T. Johnson, Europhys. Lett. **47**, 601 (1999).
[34] Z. Osváth, G. Vértesy, L. Tapasztó, F. Wéber, Z. E. Horváth, J. Gyulai, and L. P. Biró, Phys. Rev. B **72**, 045429 (2005).
[35] G. Buchs, A. V. Krasheninnikov, P. Ruffieux, P. Gröning, A. S. Foster, R. M. Nieminen, and O. Gröning, New J. Phys. **9**, 275 (2007).
[36] M. Ishigami, H. J. Choi, S. Aloni, S. G. Louie, M. L. Cohen, and A. Zettl, Phys. Rev. Lett. **93**, 196803 (2004).
[37] M. Ouyang, J. L. Huang, C. L. Cheung, and C. M. Lieber, Science **291**, 97 (2001).
[38] I. Horcas, R. Fernandez, J. M. Gomez-Rodriguez, and J. Colchero, Rev. Sci. Instrum. **78**, 013705 (2007).
[39] J. Tersoff and D. R. Hamann, Phys. Rev. B **31**, 805 (1985).
[40] Arrandee™, www.arrandee.com
[41] G. Buchs, P. Ruffieux, P. Gröning, and O. Gröning, Appl. Phys. Lett. **90**, 013104 (2007).
[42] I. W. Chiang, B. E. Brinson, A. Y. Huang, P. A. Willis, M. J. Bronikowski, J. L. Margrave, R. E. Smalley, and R. H. Hauge, J. Phys. Chem. B **105**, 8297 (2001).
[43] L. C. Venema, V. Meunier, P. Lambin, and C. Dekker, Phys. Rev. B **61**, 2991 (2000).
[44] H. Yorikawa and S. Muramatsu, Phys. Rev. B **52**, 2723 (1995).
[45] G. Kresse and J. Furthmüller, Comput. Mater. Sci. **6**, 15 (1996).
[46] G. Kresse and J. Furthmüller, Phys. Rev. B **54**, 11169 (1996).
[47] G. Kresse and D. Joubert, Phys. Rev. B **59**, 1758 (1999).
[48] P. E. Blöchl, Phys. Rev. B **50**, 17953 (1994).
[49] J. P. Perdew, J. A. Chevary, S. H. Vosko, K. A. Jackson, M. R. Pederson, D. J. Singh, and C. Fiolhais, Phys. Rev. B **46**, 6671 (1992).
[50] P. E. Blöchl, O. Jepsen, and O. K. Andersen, Phys. Rev. B **49**, 16223 (1994).
[51] S. Kümmel and L. Kronik, Rev. Mod. Phys. **80**, 3 (2008).
[52] S. Lany and A. Zunger, Phys. Rev. B **78**, 235104 (2008).
[53] C. J. Calzado, N. C. Hernandez, and Javier Fdez. Sanz, Phys. Rev. B **77**, 045118 (2008).
[54] C. Di Valentin, G. Pacchioni, and A. Selloni, Phys. Rev. Lett. **97**, 166803 (2006).
[55] L. Hedin, Phys. Rev. **139**, A796 (1965).
[56] X. Zhu and S. G. Louie, Phys. Rev. B **43**, 14142 (1991).
[57] A. D. Becke, J. Chem. Phys. **98**, 1372 (1993).
[58] C. Lee, W. Yang, and R. G. Par, Phys. Rev. B **37**, 785 (1988).
[59] V. I. Anisimov, J. Zaanen, and O. K. Andersen, Phys. Rev. B **44**, 943 (1991).
[60] S. L. Dudarev, G. A. Botton, S. Y. Savrasov, C. J. Humphreys, and A. P. Sutton, Phys. Rev. B **57**, 1505 (1998).
[61] T. W. Odom, J. L. Huang, P. Kim, and C. M. Lieber, J. Phys. Chem. B **104**, 2794 (2000).
[62] G. Buchs, P. Ruffieux, P. Gröning, and O. Gröning, Appl. Phys. Lett. **93**, 073115 (2008).
[63] A. Tolvanen, J. Kotakoski, A. V. Krasheninnikov, and K. Nordlund, Appl. Phys. Lett. **91**, 173109 (2007).
[64] A. V. Krasheninnikov, K. Nordlund, and J. Keinonen, Appl. Phys. Lett. **81**, 1101 (2002).
[65] J. Pomoell, A. V. Krasheninnikov, and K. Nordlund, J. Appl. Phys. **96**, 2864 (2004).
[66] A. J. Lu and B. C. Pan, Phys. Rev. Lett. **92**, 105504 (2004).
[67] A. V. Krasheninnikov, P. O. Lehtinen, A. S. Foster, and R. M. Nieminen, Chem. Phys. Lett. **418**, 132 (2006).
[68] S. Berber and A. Oshiyama, Phys. Rev. B **77**, 165405 (2008).
[69] A. V. Krasheninnikov, K. Nordlund, P. O. Lehtinen, A. S. Foster, A. Ayuela, and R. M. Nieminen, Phys. Rev. B **69**, 073402 (2004).
[70] A. J. Stone and D. J. Wales, Chem. Phys. Lett. **128**, 501 (1986).
[71] M. T. Lusk and L. D. Carr, Phys. Rev. Lett. **100**, 175503 (2008).
[72] A. V. Krasheninnikov, K. Nordlund, and J. Keinonen, Phys. Rev. B **65**, 165423 (2002).

[73] M. Buongiorno Nardelli, B. I. Yakobson, and J. Bernholc, Phys. Rev. B **57**, R4277 (1998).
[74] B. I. Yakobson, C. J. Brabec, and J. Bernholc, Phys. Rev. Lett. **76**, 2511 (1996).
[75] A. V. Krasheninnikov, K. Nordlund, M. Sirviö, E. Salonen, and J. Keinonen, Phys. Rev. B **63**, 245405 (2001).
[76] A. V. Krasheninnikov and K. Nordlund, J. Vac. Sci. Technol. B **20**, 728 (2002).
[77] D. Orlikowski, M. Buongiorno Nardelli, J. Bernholc, and C. Roland, Phys. Rev. Lett. **83**, 4132 (1999).
[78] V. Meunier and P. Lambin, Carbon **38**, 1729 (2000).
[79] A. Rubio, Appl. Phys. A: Mater. Sci. Process. **68**, 275 (1999).
[80] A. V. Krasheninnikov and V. F. Elesin, Surf. Sci. **454-456**, 519 (2000).
[81] A. A. El-Barbary, R. H. Telling, C. P. Ewels, M. I. Heggie, and P. R. Briddon, Phys. Rev. B **68**, 144107 (2003).
[82] A. V. Krasheninnikov, Solid State Commun. **118**, 361 (2001).
[83] V. M. Pereira, F. Guinea, J. M. B. Lopes dos Santos, N. M. R. Peres, and A. H. Castro Neto, Phys. Rev. Lett. **96**, 036801 (2006).
[84] J. G. Kushmerick, K. F. Kelly, H.-P. Rust, N. J. Halas, and P. S. Weiss, J. Phys. Chem. B **103**, 1619 (1999).
[85] A. R. Rocha, J. E. Padilha, A. Fazzio, and A. J. R. da Silva, Phys. Rev. B **77**, 153406 (2008).
[86] G. Buchs, Ph.D. thesis, University of Basel, Basel, 2008.
[87] M. Berthe *et al.*, Nano Lett. **7**, 3623 (2007).
[88] D. Orlikowski, M. Buongiorno Nardelli, J. Bernholc, and C. Roland, Phys. Rev. B **61**, 14194 (2000).
[89] Y. Gan, J. Kotakoski, A. V. Krasheninnikov, K. Nordlun, and F. Banhart, N. J. Phys. **10**, 023022 (2008).
[90] R. G. Amorim, A. Fazzio, A. Antonelli, F. D. Novaes, and A. da Silva, Nano Lett. **7**, 2459 (2007).
[91] G. D. Lee, C. Z. Wang, E. Yoon, N. M. Hwang, D. Y. Kim, and K. M. Ho, Phys. Rev. Lett. **95**, 205501 (2005).
[92] J. Kotakoski, A. V. Krasheninnikov, and K. Nordlund, Phys. Rev. B **74**, 245420 (2006).
[93] A. V. Krasheninnikov, A. S. Foster, and R. M. Nieminen, Phys. Rev. Lett. **99**, 179703 (2007).
[94] C. P. Ewels, R. H. Telling, A. A. El-Barbary, M. I. Heggie, and P. R. Briddon, Phys. Rev. Lett. **91**, 025505 (2003).
[95] P. O. Lehtinen, A. S. Foster, A. Ayuela, T. T. Vehviläinen, and R. M. Nieminen, Phys. Rev. B **69**, 155422 (2004).
[96] A. N. Andriotis, M. Menon, R. M. Sheetz, and L. Chernozatonskii, Phys. Rev. Lett. **90**, 026801 (2003).
[97] S.-W. Hla, K.-F. Braun, and K.-H. Rieder, Phys. Rev. B **67**, 201402(R) (2003).
[98] S.-W. Hla, K.-F. Braun, B. Wassermann, and K.-H. Rieder, Phys. Rev. Lett. **93**, 208302 (2004).
[99] A. Högele, C. Galland, M. Winger, and A. Imamoglu, Phys. Rev. Lett. **100**, 217401 (2008).